Towards optimization of a wave-to-wire energy device in a breakwater contraction

Jonathan M. Bolton, Onno Bokhove, Duncan J. Borman, Anna Kalogirou, and Harvey M. Thompson

***Abstract*—A wave-to-wire mathematical and numerical model is explored for a wave-energy device ideally integrated within a breakwater. It consists of a wave-focussing contraction, a wave-activated buoy and an electromagnetic power generator. The model with all its integrated components has previously been derived from first principles in wave hydrodynamics, constrained (vertical) buoy motion and the 3D Maxwell equations for the electromagnetic generator (the latter using the axisymmetry of the set-up and thin-wire approximations). By revisiting this model, the following novelties are presented: (i) dispersive long-wave dynamics is included at similar computational costs as, and in extension of, the nondispersive shallow-water dynamics considered numerically hitherto, via inclusion of so-called Benny-Luke wave dynamics; (ii) improvements have been made to modelling the power generator and the numerical formulation of the coupled, monolithic system of wave-, buoy and electro-dynamics; and, (iii) a series of simulations of the new shallow-water and Benney-Luke wave-energy models are presented, exploring the resonance characteristics of the system under varying wave amplitudes and frequencies. It turns out that it is better to directly use a potential flow model because it can be made consistent like the shallow-water model, whereas the Benney-Luke model cannot. Finally, it is discussed how the modelling set-up is well-suited for further optimization using both the reduced wave-energy model as well as surrogate modelling.**

***Index Terms*—wave-to-wire model, dispersive wave dynamics, amplitude-frequency resonance characteristics**

I. Introduction

OCEAN waves produced by wind action are a major potential source of energy. However, extracting this energy is complicated by a number of factors, including complex diffraction and radiation phenomena, the need to account for variability in energy availability and survivability in extreme conditions. As reported in several reviews of wave-energy conversion (see e.g. [1]), numerous investigations have explored the feasibility and practicality of wave-energy converters, with a key consideration being that of matching the resonant frequency of the converter to the frequency of the incoming waves.

Paper ID: 2191. EWTEC track: Wave device development and testing. This research forms part of JB's PhD, funded by the EPSRC under grant EP/S022732/1.

J. Bolton: EPSRC Centre for Doctoral Training in Fluid Dynamics at Leeds and Leeds Institute for Fluid Dynamics, University of Leeds, Leeds, LS2 9JT, UK; j.m.bolton@leeds.ac.uk

O. Bokhove: Leeds Institute for Fluid Dynamics, University of Leeds; o.bokhove@leeds.ac.uk

D. Borman: School of Civil Engineering, University of Leeds; d.j.borman@leeds.ac.uk

A. Kalogirou: School of Mathematical Sciences, University of Nottingham, Nottingham, NG7 2RD, UK; anna.kalogirou@nottingham.ac.uk

H. Thompson: School of Mechanical Engineering, University of Leeds; h.m.thompson@leeds.ac.uk

These practical complexities have resulted in the development of a wide variety of wave-energy technologies which rely upon a range of mechanisms for absorbing energy from the waves. These include Oscillating Water Columns (OWCs) and Oscillating and Heaving Body systems, such as the Salter Duck and Swinging Mace systems that emerged from the University of Edinburgh [2]. Overtopping Converters (OTCs), which convert the potential energy difference between water in a reservoir and the ambient surroundings into electrical energy using hydraulic turbines, are also common. Of particular relevance to the present study is the TapChan (Tapered Channel Wave Power) OTC device, which comprises a collector, converter, water reservoir and low-head water turbine [3]. Its gradually narrowing channel amplifies the incoming waves before they enter the converter, causing more water to spill over the wall and fill the reservoir, thus increasing the power output.

The present study focusses on the novel device proposed and developed by Bokhove et al. [4], [5], following their experimental and numerical study of extreme nonlinear water wave amplification in a contraction, where they observed up to a tenfold amplification of an incoming soliton compound. The device consists of a channel with a V-shaped contraction, in which a buoy is placed. Attached to the buoy is a magnet (or a set of multiple magnets) which, by constraining the buoy to move along a fixed trajectory, travels through a fixed induction coil when the buoy is displaced by the waves. This electromagnetic induction system forms a power take-off (PTO) mechanism and creates electrical energy. Out of the ocean, a tank with a wavemaker is used to generate and contain the waves, with Fig. 1 showing several views of the tank and buoy.

The device is suitable for breakwaters and docks, and was inspired by features of three existing devices, namely the aforementioned TapChan, the Interproject Service (IPS) Heaving Buoy [6] and an OWC with a vertical blowhole through which rapid air flow is generated [7]. It also has similarities with the Berkeley Wedge [8], which has a comparable PTO mechanism without amplitude-enhancing contraction.

In addition to demonstrating a proof-of-concept of the device, seen in a video [9], Bokhove et al. [4], [5] developed a complementary and fully coupled nonlinear mathematical model of the combined 3D potential-flow hydrodynamics, wave-activated buoy kinematics and electromagnetic power generation, cf. other wave-to-wire models [10]. The governing equations were derived using a single, concise variational principle, an approach new to the fields of wave and tidal

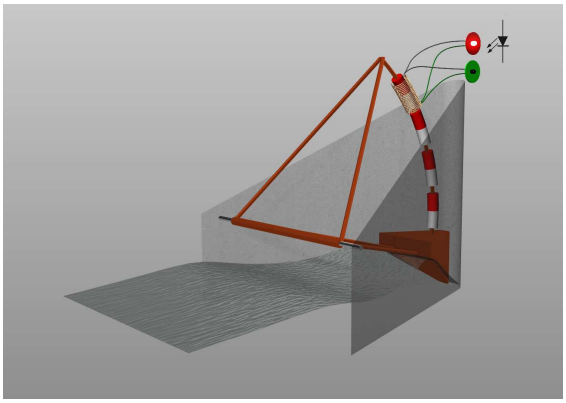

(a) Artistic rendering of the device in the contraction with PTO and loads, as well as an incoming wave.

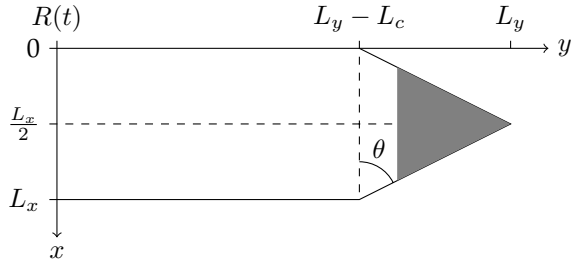

(b) Top view of the tank and buoy, outlining the tank's dimensions and how the buoy fits the shape of the contraction.

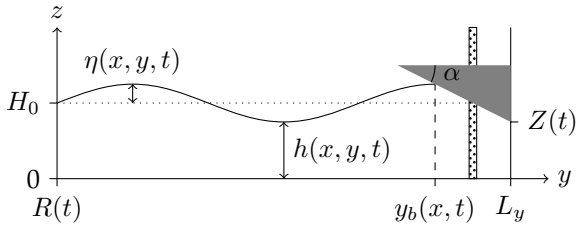

(c) Side view at time t, with the buoy constrained to move vertically.

Fig. 1. (a) Artistic rendering with the slightly arced mast, attached red-white magnets, the coils and LED loads shown in red and green (image courtesy Wout Zweers). The arced mast is modelled as a straight one. Sketches of the top (b) and side (c) views buoy (shaded). The notation is defined in Section II. Values for the wavetank used are: $L_x = 0.2\text{m}, L_y = 2.0\text{m}, H_0 = 0.1\text{m}, L_c = 0.25\text{m}$.

energy and introduced at EWTEC19. They generated numerical solutions to the linearised coupled equations using the 2D shallow-water (SW) approximation (for increased numerical efficiency) and investigated the effect of induction coils, buoy mass and wavemaker frequency upon the amount of power generated, providing the first study of the resonant behaviour and parameter dependence of the device.

This paper extends the previous studies through the use of a 2D Benney-Luke (BL) approximation of the 3D system of potential-flow equations. For higher-order dispersive waves, the BL approximation has increased accuracy relative to the SW approximation, while retaining the improvement in numerical efficiency relative to the full 3D potential-flow system. Using hydrodynamic wave models with such intermediate complexity forms a key step towards the ultimate goal of using accurate and efficient numerical methods within an effective overall numerical optimisation strategy for maximising the device's power output subject to practical operating constraints, see e.g. [11].

The paper outline is as follows. In Section II the nonlinear wave-energy system and governing BL equations are introduced. In Section III the system is linearised and discretised. Section IV presents numerical results exploring the improvements afforded by the BL approximation vis-à-vis the SW equations. Conclusions and discussion follow in Section V.

II. Problem specification

The device can be divided into three constituent subsystems, namely: the BL-approximated hydrodynamics, driven by the motion of the wavemaker; the motion of the buoy, driven by the movement of the water beneath it; and, the power generated by the electromagnetic induction system, itself driven by the movement of the buoy. The first two sub-systems are coupled through the buoy-water interface, and there is a two-way coupling between the buoy's motion and the current in the coil, with the current applying a magnetic force back onto the buoy. Mathematical descriptions of the three sub-systems are given next, followed by a brief outline of the BL approximation process. Finally, the 2D system of equations for the fully-coupled and BL-approximated system is presented.

A. Tank and buoy

Fig. 1 shows an artistic rendering of the device and outlines the geometry of the tank and buoy. The tank has width L_x and length L_y, with the V-shaped wall given by

$$y = l_y(x) = L_y - L_c \left| 1 - \frac{2x}{L_x} \right|,$$

where L_c is the length of the contraction, which is at an angle of θ to the x-z plane. The water in the tank has velocity $\mathbf{u}(x, y, z, t)$ and constant density ρ_0, and fills the region

$$x \in [0, L_x], \quad y \in [R(t), l_y(x)], \quad z \in [0, h(x, y, t)],$$

where $y = R(t)$ is the (prescribed) position of the wavemaker and $z = h(x, y, t)$ is the variable position

of the (single-valued) water surface. Using the overdot short-hand to denote a time-derivative, the wavemaker's velocity is $\dot{R}(t)$.

The buoy is a tetrahedron, with: a flat top; two sides, perpendicular to the top, that fit along the walls of the contraction; and, a slanted hull at an angle α to the top. Its mass, including an attached rod and magnet, is M. The buoy can be constrained to travel in the vertical (Fig. 1c) or along an arc, with the latter having two advantages: a rotating axle is more durable than the bearings on a vertical rod, while holding the pivot fixed with the buoy sustained above the water means it can be taken out of action in a storm. Since the mathematics of the arced trajectory is more involved, only vertical motion is considered presently.

The buoy's position along this trajectory is $z = Z(t)$ and is measured to be where its nadir lies (as in Fig. 1c), with $W(t) = \dot{Z}$ its velocity (pertaining to surge and heave). The position of the hull is given by $z = h_b(y,t)$ and the waterline by $y = y_b(x,t)$. Beyond this, for $y > y_b$, the surface of the water is constrained to match the hull's shape, i.e

$$h = h_b \text{ for } y > y_b, \text{ or } (h - h_b)\Theta(y - y_b) = 0,$$

where Θ is the Heaviside step function, defined to be zero for $y \leq y_b$ and unity for $y > y_b$. For all t, the angle of the hull to the horizontal remains the same, so

$$h_b(y,t) \equiv h_b(y, Z(t)) = Z(t) + (L_y - y)\tan\alpha.$$

(More complex shapes can be considered as well as non-shallow configurations, which would require either coordinate transformations or moving meshes.)

At $t = 0$, the water, wavemaker and buoy are at rest (so $\mathbf{u}|_{t=0} = 0$, $\dot{R}(0) = 0$ and $W(0) = 0$), the wavemaker is at $R(0) = 0$, the waterline is at $y_b(x,0) = L_b$, the (unconstrained) free-surface height is H_0 and the buoy rests at $Z(0) = Z_0$. The at-rest hull position is therefore

$$h_b|_{t=0} \equiv h_b|_{z=Z_0} \equiv H_b(y) = Z_0 + (L_y - y)\tan\alpha, \quad (1)$$

and the position of the surface can be written as

$$h|_{t=0} \equiv H(y) = \begin{cases} H_0 & y \leq L_b, \\ H_b(y) & y \geq L_b. \end{cases} \quad (2)$$

By considering the partially-submerged portion of the buoy and using that H is continuous at the waterline, unknowns Z_0 and L_b can be written in terms of known parameters via Archimedes' principle. From [5], they are given by

$$Z_0 = H_0 - \left(\frac{3M\tan\theta\tan^2\alpha}{\rho_0}\right)^{\frac{1}{3}}$$

and

$$L_b = L_y - \left(\frac{3M\tan\theta}{\rho_0\tan\alpha}\right)^{\frac{1}{3}}.$$

B. Magnet and coil

A mast is fixed onto the top of the buoy, with a cylindrical magnet (or multiple magnets) of (total) magnetic dipole moment m and length L_m attached to it. The magnet is aligned vertically and spans the time-dependent region

$$z \in [Z(t) + H_m - L_m/2, Z(t) + H_m + L_m/2],$$

with H_m the distance between the nadir of the buoy and the magnet's centre. The induction coil, of length L, is also aligned vertically and is coaxial to the magnet, but is fixed at such a height that its centre is offset from the magnet's centre when the system is at rest. That is, the coil spans the fixed region

$$z \in [Z_0 + (1 + \alpha_h)H_m - L/2, Z_0 + (1 + \alpha_h)H_m + L/2],$$

with $\alpha_h H_m$ the offset and $\alpha_h \neq 0$. This offset ensures that, upon linearising, the buoy and induction system remain coupled (see Section III). The coil has n_c loops, radius a (greater than the magnet's radius) and resistance R_c.

The coil has inductance L_i and forms part of a circuit, which circuit has resistance R_i. The movement of the magnet causes a current $I(t)$ to flow through the coil via electromagnetic induction, with charge $Q(t)$ satisfying $\dot{Q} = I$. At rest, the magnet is stationary and there is no ambient current or charge, so $I(0) = 0$ and $Q(0) = 0$. The voltage driven by the movement of the magnet, which can be calculated using Faraday's and Ohm's laws (see [5]), is $\gamma G(Z)\dot{Z}$. The function $G(Z)$ acts to apply the magnetic field of the magnet to the coil and γ is a constant corresponding to the size and strength of the electromagnet given by

$$\gamma = \mu_0 m a^2 n_c/(2L),$$

where $\mu_0 \approx 4\pi \times 10^{-7}\,\mathrm{H\,m^{-1}}$ is the permeability of free space. In the far-field approximation, $G(Z)$ given by

$$G(Z) \approx \frac{1}{(a^2 + [Z_0 + \alpha_h H_m - Z + L/2]^2)^{3/2}} - \frac{1}{(a^2 + [Z_0 + \alpha_h H_m - Z - L/2]^2)^{3/2}}. \quad (3)$$

The full expression of (3) is found in (5) of [4] and (44f) of [5], with Fig. 3 of [4] showing that the far-field approximation is valid despite the coil being in close proximity to the magnet.

To enable monitoring of the power output, the circuit contains a component which draws out a voltage $V(Q,I) \equiv V(t)$ and turns it into electrical power $P(t) = I(t)V(t)$, with the mean power output between time $t = 0$ and $t = T$ given by $\hat{P} = \frac{1}{T}\int_0^T P(t)\,\mathrm{d}t = \frac{1}{T}\int_0^T I(t)V(t)\,\mathrm{d}t$. As in [4], [5], one pair of LEDs (circuited in parallel and in opposite directions) is used here. Its voltage is modelled by the adapted Shockley equation

$$V = -\mathrm{sign}(I) n_q V_T \ln(1 + |I|/I_{sat}), \quad (4)$$

with n_q the quality factor, V_T the thermal voltage and I_{sat} the saturation current. Note that (4) does not depend on Q and $V = 0$ when $I = 0$. To model large-scale harvesting, multiple pairs of LEDs can be used. Alternatively, batteries can be modelled via (modified) Shepherd models (e.g. [12]), likely needing AC-DC conversion via a rectifier. In this case, V would depend on both Q and I.

In the system of equations presented in Section II-D, the conjugate momentum of Q, denoted $P_Q(t)$ and defined as

$$P_Q = L_i\dot{Q} - K(Z) \text{ with } K(Z) \equiv \gamma \int_0^Z G(\mathcal{Z})\,\mathrm{d}\mathcal{Z},$$

is first used instead of I. This allows a consistent, geometric time-discretisation to be formed (see Section III). Given P_Q and Z, the current $I = \dot{Q} = (P_Q + K(Z))/L_i$.

C. Benney-Luke wave dynamics

As an alternative to the 3D potential-flow hydrodynamics derived in [5], a 2D Benney-Luke (BL) approximation can be formed. First introduced by Benney and Luke in [13], the BL approximation is valid for weakly nonlinear waves with long wavelengths. The approximation enables the effective removal of the vertical coordinate in exchange for terms with higher-order derivatives, which capture dispersive gravity waves. Compared to the 2D shallow-water (SW) approximation used in [4], [5], this provides similar benefits in terms of computational cost with increased accuracy.

In potential-flow theory, the hydrodynamics are assumed to be irrotational, incompressible and inviscid, and are governed by a mathematical description of two fields: the velocity potential $\phi(x, y, z, t)$ satisfying $\mathbf{u} = \nabla\phi$ and the (single-valued) water depth $h(x, y, t)$. The incompressibility assumption then requires the potential to satisfy the Laplace equation $\nabla \cdot \mathbf{u} = \nabla^2\phi = 0$ in the entire 3D domain. Assuming a flat bottom and no wave breaking, such that h denotes the height of the free surface, the prognostic Bernoulli and kinematic equations govern the dynamics of the velocity potential at the free surface and the free-surface height itself.

The BL approximation of these three equations proceeds as follows. First, the variables x, y, z and t and the hydrodynamic fields ϕ and h are non-dimensionalised using so-called BL scalings (given in e.g. [14], [15]). For the present application, this non-dimensionalisation is then extended to include the non-standard wavemaker and buoy functions, which are coupled directly to the hydrodynamics. Since the electromagnetic terms do not directly impact upon the hydrodynamics, these terms can be neglected while deriving the approximation and can be recovered afterwards, with no changes relative to the shallow-water case.

Using these BL scalings, a dimensionless Laplace equation and boundary conditions (BCs) for the potential are obtained, which are used to write the (non-dimensional) potential as an asymptotic expansion of a z-invariant function in powers of z^2, i.e.,

$$\phi(x, y, z, t) = \Phi(x, y, t) - \frac{\mu z^2}{2}\nabla^2\Phi + \mathcal{O}(\mu^2 z^4), \tag{5}$$

with $\Phi \equiv \phi|_{z=0}$ the potential at the bottom of the tank and $\mu \ll 1$ a dimensionless dispersion/long-wavelength parameter. This expansion is then placed into the dimensionless form of the 3D Lagrangian presented in [4], [5] with terms of order μ^2 and above neglected, and the explicit z-dependence is then integrated out. The resulting 2D Lagrangian is re-dimensionalised and given in (A.1). The 2D system of equations derived from this Lagrangian is presented next.

D. Wave-to-wire dynamics

The system of equations for the entire, coupled wave-to-wire device under the BL approximation can be generated by taking the variation of a single Lagrangian, or variational principle, given in (A.1), augmented with circuit losses in the electromagnetic generator and the energy output harvested by the LEDs. The resulting 2D system, including the novel BL wave dynamics, reads:

BL Bernoulli & kinematic equations:

$$\frac{\partial\Phi}{\partial t} - \underline{\frac{H_0^2}{2}\frac{\partial}{\partial t}\left(\nabla^2\Phi\right)} + \frac{1}{2}\|\nabla\Phi\|^2 + g(h - H_0) + \lambda\Theta(y - y_b) = 0, \tag{6a}$$

$$\frac{\partial h}{\partial t} - \underline{\frac{H_0^2}{2}\frac{\partial}{\partial t}\left(\nabla^2 h\right)} + \nabla\cdot(h\nabla\Phi) - \underline{\frac{2H_0^3}{3}\nabla^4\Phi} = 0, \tag{6b}$$

Buoy dynamics:

$$\dot{Z} = W, \tag{6c}$$

$$\dot{W} = -g - \frac{\gamma G(Z)(P_Q + K(Z))}{ML_i} + \frac{\rho_0}{M}\int_0^{L_x}\int_{y_b}^{l_y}\lambda\,\mathrm{d}y\,\mathrm{d}x, \tag{6d}$$

Electromagnetic generator:

$$\dot{Q} = \frac{P_Q + K(Z)}{L_i} \equiv I, \tag{6e}$$

$$\dot{P}_Q = -\frac{(P_Q + K(Z))(R_c + R_i)}{L_i} + V(I), \tag{6f}$$

Free-surface-equals-buoy-shape constraint:

$$h = h_b = Z + (L_y - y)\tan\alpha \text{ for } y > y_b(x, t), \tag{6g}$$

Boundary conditions (for nonlinear system):

$$\lambda = 0 \text{ at } y = y_b(x, t), \tag{6h}$$

$$\frac{\partial\Phi}{\partial y} = \dot{R} \text{ at } y = R(t), \tag{6i}$$

$$\nabla\Phi\cdot\hat{\mathbf{n}} = 0 \text{ on } \Sigma_w, \tag{6j}$$

$$\nabla\left(\nabla^2\Phi\right)\cdot\hat{\mathbf{n}} = 0 \text{ on } \Sigma, \tag{6k}$$

$$\frac{\partial}{\partial t}\left(\nabla h\cdot\hat{\mathbf{n}}\right) = 0 \text{ on } \Sigma, \tag{6l}$$

with the operator $\nabla \equiv (\partial/\partial x, \partial/\partial y)$ now holding in 2D, Σ denoting all five vertical tank walls (including the wavemaker) and Σ_w the four stationary walls (excluding the wavemaker). The system includes three pairs of equations relating to the device's three components, each of which govern the rate-of-change of a pair of conjugate variables.

The first pair of equations are the Bernoulli and kinematic conditions at the free surface $z = h$, formulated with the bottom potential Φ and fluid depth h. Note that within BL, the valid *dimensional* free-surface potential is $\Psi = \Phi - (H_0^2/2)\nabla^2\Phi$. The Bernoulli equation is coupled to the wetted part of the buoy (where $y > y_b$) via the Lagrange multiplier λ and Heaviside function $\Theta(y - y_b)$.

The second pair of equations govern the position and velocity of the buoy. (6d) is Newton's second law, involving the gravitational force $-Mg$, the electromagnetic force applied by the induction motor above (second term on the RHS) and the force applied by the water below (final term). The Lagrange multiplier λ in the final term is thus seen to be the hydrodynamic pressure under the buoy, whose BC (6h) is found by imposing constant density weakly rather than strongly (see [5] for details).

The third pair of equations concern the electromagnetic power generator. Note that without the resistance $R_c + R_i$ and voltage output V on the RHS of (6f), the conjugate momentum P_Q is conserved, i.e. $\dot{P}_Q = 0$.

When compared to the SW approximation used in [4], [5], the additional underlined terms in the BL Bernoulli and kinematic equations introduce long-wave dispersion to the problem, which is otherwise absent in the SW system. There are additional BCs on $\nabla^2\Phi$ and h, introduced by the second term in (5) and required due to the introduction of fourth-order spatial derivatives by the final term of the Bernoulli equation. The order of these derivatives can be reduced by introducing an auxiliary variable $q = -{}^2\!/_3\nabla^2\Phi$, with the BC $\nabla q \cdot \hat{\mathbf{n}} = 0$ on Σ replacing (6k). This reduction of order is relevant in the numerical discretisation discussed shortly.

III. Linearisation and discretisation

A. Linearisation

As a stepping-stone towards nonlinear modelling, we first linearise the new system and perform a preliminary optimisation of the PTO-system, therefore assessing effects of the dispersive hydrodynamic terms in an optimisation. System (6) is linearised about a rest-state using the following decompositions:

$$\begin{aligned}
\Phi(x,y,t) &= 0 + \widetilde{\Phi}(x,y,t), & Z(t) &= Z_0 + \widetilde{Z}(t),\\
h(x,y,t) &= H(y) + \eta(x,y,t), & W(t) &= 0 + \widetilde{W}(t),\\
\lambda(x,y,t) &= \Lambda(y) + \widetilde{\lambda}(x,y,t), & Q(t) &= 0 + \widetilde{Q}(t),\\
y_b(x,t) &= L_b + \widetilde{y}_b(x,t), & I(t) &= 0 + \widetilde{I}(t),\\
P_Q(t) &= -K(Z_0) + \widetilde{P}_Q(t), & R(t) &= 0 + \widetilde{R}(t),
\end{aligned} \tag{7}$$

where $\Lambda(y) = g(H_0 - H_b(y))$ follows from evaluating (6a) at rest for $y > y_b$, and $I(0) = 0$ implies $P_Q(0) = -K(Z_0)$. All of the rest-state variables cancel out, while Taylor-expansions can be applied throughout to separate terms linear in the displacement variables from higher-order terms. It is then assumed that the displacements are small, such that any higher-order terms can be neglected. In this linearised limit, the moving boundaries at $y = R(t)$ and $y = y_b(x,t)$ become stationary boundaries at $y = 0$ and $y = L_b$, respectively.

In particular, an explicit expression for the waterline displacement $\widetilde{y}_b$ is found from (6g) to be (see [5])

$$\widetilde{y}_b = (\widetilde{Z} - \eta|_{y=L_b^-})/\tan\alpha, \tag{8}$$

giving that the position of the waterline is not an independent variable but instead depends on the positions of the buoy and free-surface. Relation (8) can be used as post-processing to display the waterline dynamics.

Upon dropping tildes, the linearised form of (6) is:

$$\frac{\partial\Phi}{\partial t} - \underline{\frac{H_0^2}{2}\frac{\partial}{\partial t}\left(\nabla^2\Phi\right)} + g\eta + \lambda\Theta(y - L_b) = 0, \tag{9a}$$

$$\frac{\partial\eta}{\partial t} - \underline{\frac{H_0^2}{2}\frac{\partial}{\partial t}\left(\nabla^2\eta\right)} + \nabla\cdot(H\nabla\Phi) + \underline{H_0^3\nabla^2 q} = 0, \tag{9b}$$

$$\underline{q + \frac{2}{3}\nabla^2\Phi = 0}, \tag{9c}$$

$$\dot{Z} = W, \tag{9d}$$

$$\dot{W} = -\frac{\gamma G(Z_0)\left(P_Q + \gamma G(Z_0)Z\right)}{ML_i} + \frac{\rho_0}{M}\int_0^{L_x}\int_{L_b}^{l_y}\lambda\,\mathrm{d}y\,\mathrm{d}x, \tag{9e}$$

$$\dot{Q} = \frac{P_Q + \gamma G(Z_0)Z}{L_i} \equiv I, \tag{9f}$$

$$\dot{P}_Q = -\frac{(P_Q + \gamma G(Z_0)Z)(R_c + R_i + R_l)}{L_i}, \tag{9g}$$

$$\eta = Z \text{ for } y \geq L_b, \tag{9h}$$

$$\lambda = g(\eta|_{y=L_b} - Z) \text{ at } y = L_b, \tag{9i}$$

$$\frac{\partial\Phi}{\partial y} = \dot{R} \text{ at } y = 0, \tag{9j}$$

$$\nabla\Phi\cdot\hat{\mathbf{n}} = 0 \text{ on } \Sigma_w, \tag{9k}$$

$$\nabla q\cdot\hat{\mathbf{n}} = 0 \text{ on } \Sigma, \tag{9l}$$

$$\nabla\eta\cdot\hat{\mathbf{n}} = 0 \text{ on } \Sigma, \tag{9m}$$

where $V(I) \approx R_l I$ for small I with $R_l = n_q V_T/I_{sat}$ an effective resistance arising from the LEDs. The boundary condition on the displacement of λ (9i) arises after Taylor-expanding (6h) and using (8) (see [5]). The linearisation of the PTO part of the model can be related to the one in [16].

Consider (9e) and (9g). The (linearised) coupling term $\gamma G(Z_0)Z$ between the buoy's displacement and the electromagnetic generator involves $G(Z_0)$. The coil's centre is offset ($\alpha_h \neq 0$, recall Section II) to ensure that $G(Z_0) \neq 0$.

An integro-elliptic equation for λ is derived by differentiating the free-surface-equals-buoy-shape constraint (9h) twice in time and using other equations to manipulate the result. This equation is given by

$$\begin{aligned}
\nabla\cdot\left[H\nabla\lambda + \underline{H_0^2\left(\frac{3H}{4} - H_0\right)\nabla\left(\frac{\partial q}{\partial t}\right)}\right]\\
- \frac{\rho_0}{M}\int_0^{L_x}\int_{L_b}^{l_y}\lambda\,\mathrm{d}y\,\mathrm{d}x = -\nabla\cdot(gH\nabla\eta)\\
- \frac{\gamma G(Z_0)\left(P_Q + \gamma G(Z_0)Z\right)}{ML_i},
\end{aligned} \tag{10}$$

for $y > L_b$. In the SW limit, the underlined term is absent (as in (23h) of [5]) and (10) can be solved given η, P_Q, Z and the BCs (9i) and $\nabla(\lambda+\eta)\cdot\hat{\mathbf{n}} = 0$ on $\Sigma|_{y>L_b}$. However, in the present case (10) needs to be coupled with an equation for $\partial_t q$, found by differentiating (9c) in time and using (9a), yielding:

$$\frac{\partial q}{\partial t} - \frac{H_0^2}{2}\frac{\partial}{\partial t}\left(\nabla^2 q\right) - \frac{2}{3}\nabla^2\left(\lambda\Theta(y - L_b)\right) = \frac{2}{3}g\nabla^2\eta, \tag{11}$$

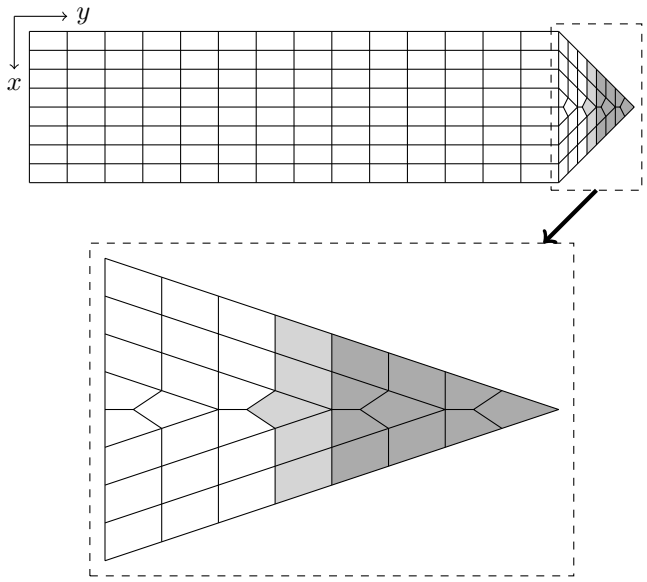

Fig. 2. An example of the mesh used in the simulations. A semi-regular structured mesh is used in the contraction, making use of only quadrilateral element shapes. The linearised/rest-state waterline $y = L_b$ lies along one of the straight lateral (x-direction) grid lines. To the right of this line (dark gray) is where the wetted part of the buoy lies. The first column of elements to the left of the waterline is shaded in light gray, used for the consistent solution of λ.

for all y. These equations serve as consistency conditions, ensuring that the constraint and its two time-derivatives are maintained over time.

B. Discretisation

The system (9), with (9h) replaced by (10) and (11), will be discretised in both space and time. The spatial discretisation employed is the finite element method (FEM) with continuous, piecewise-linear Lagrange basis functions, while the symplectic Euler time-stepping scheme [17, p. 189] is used to ensure that the coupling constraint (9h) is kept consistent over time. Hence, the spatial discretisation is formally second-order, while the time-stepping scheme is formally first order.

This geometrically compatible numerical method ensures that, in the absence of dissipative elements (i.e. when $\dot{P}_Q = 0$) and when the wavemaker is turned off, such that the entire system is energy-conserving, oscillations in the numerical energy are bounded. These oscillations disappear when the time-step Δt is decreased to zero, guaranteeing proper and consistent energy transfer between the three subsystems.

An example of the quadrilateral spatial mesh used is found in Fig. 2. It contains $N_x \times N_y$ elements in the rectangular region and $N_x(N_x + 1)/2$ elements in the contraction, with N_x required to be even. The total number of nodes is thus $N_n = (N_x + 1)(N_y + 1) + N_x(N_x + 2)/2$, and the various parameters defining the mesh and tank geometry are chosen such that the linearised/rest-state waterline lies along one of the straight lateral (x-direction) grid lines (i.e. one without a kink around the kite-shaped element seen along the centre-line).

To utilise the FEM, a consistent weak formulation of the spatially-dependent equations needs to be produced. This is done by multiplying each equation by a suitable test function $\varphi(x, y)$ and integrating in space, with any second-order derivatives removed via suitable integration-by-parts and boundary conditions. These spatially-continuous integral equations are then discretised on the mesh by taking the test function at each node k to be the Lagrange basis function $\varphi_k(x, y)$. Subsequently, the spatially-dependent variables inside the integrals are approximated by the sum over all nodes of unknown, time-dependent coefficients multiplied by the known, time-independent basis functions - e.g. $\Phi(x, y, t) \approx \Phi_l(t)\varphi_l(x, y)$, with the repeated index l implying the sum. The coefficients are taken outside of the spatial integrals, which can then be explicitly evaluated since the basis functions are known. Vectors of the coefficients then become the unknown variables being solved for, with the evaluated integrals becoming so-called "mass" and "stiffness" matrices.

The entire system of continuous, spatially-dependent differential equations then becomes a system of individual linear (matrix-vector) systems, which can be readily solved on a computer. The basis functions are defined to only span neighbouring elements, such that the matrices are sparse. In the present work, as in [4], [5], these matrices are explicitly calculated and inverted using MATLAB. Implementation in the more versatile, Python-based, finite-element environment *Firedrake* [18] is in progress. Consistency relations (10) and (11) need to met also by the discretisation, which could be proven for the (linear) shallow-water and full potential flow system but not for the intermediate-complexity BL-system, due to the presence of the underlined time-derivative terms in (9a) and (9b). Further discretisation details are found in Appendix B.

IV. Preliminary optimisation results

The results of two model systems are investigated: the linearised BL-system (9) and the limiting linearised shallow-water system (i.e., (9) without the underlined terms). The BL model is solved in two ways: either the consistency relations are solved as a discrete system with λ and $\partial_t q$ as coupled unknowns, or numerically as one equation for λ. The shallow-water model is solved in one way. For the BL-system, the two solution techniques lead to highly similar results, while there are some differences for the shallow-water solutions, in the latter case only one equation for λ needs solving. Constraints are obeyed up to machine precision in the shallow-water case, but for the two BL-solutions (system/one equation solve), the primary constraint $\eta - Z = 0$ and secondary constraint $\partial_t \eta - W = 0$ on $y > L_b$ are obeyed up to circa order 10^{-6}.

Resonance is investigated as function of wavemaker frequency ω_i and wavemaker amplitude A_i for harmonic waves. The wavemaker $R(t) = A_i \sin \omega_i t$. The parameter values are as in Table 5 of [5] with the following differences and additions:

$$H_0 = 0.1\text{m},\ M = 0.1\text{kg},\ \alpha = 0.3655\text{rad},$$
$$L_x = 0.2\text{m},\ L_y = 2.0\text{m},\ d = 0.27\text{m},$$
$$L_c = \sqrt{d^2 - \tfrac{1}{4}L_x^2} = 0.2508,$$

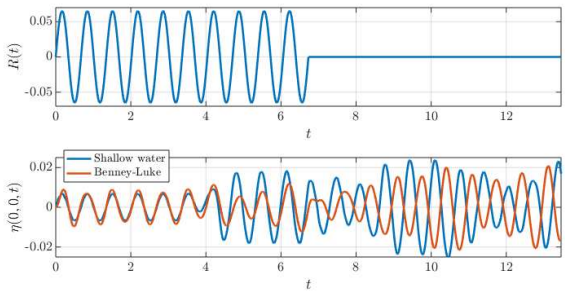

Fig. 3. Wavemaker output and free surface evolution (in m) at $y = 0$ as function of time t (in s). The wavemaker is on for $T_w = 10$ periods and then switched off with time shown for $2T_w$. The fastest, shallow-water reflected waves arrive back at the wavemaker at approximately $t = 4$s but due to dispersion slowing down shorter waves this is less prominent in the BL-system. $A = 0.0653$m and $\omega = 9.33$Hz.

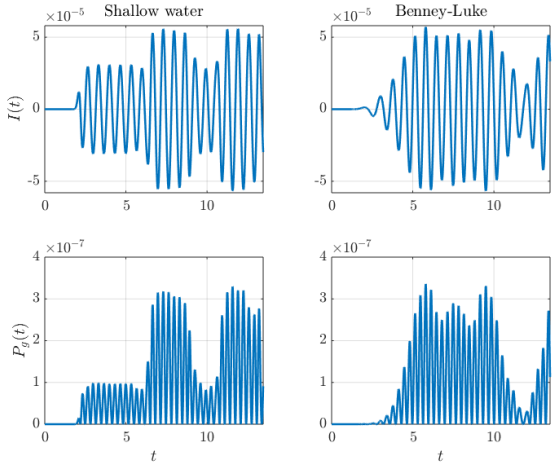

Fig. 4. Generated current I (in Ampere) and power P_g (in Volt×Ampere) as functions of time t (in seconds), obtained in the case of shallow water (left-hand panels) or from the Benney-Luke system (right-hand panels).

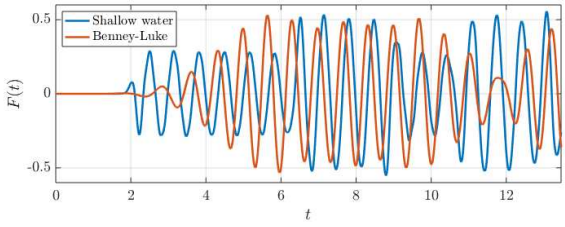

Fig. 5. Evolution of the force on the buoy's surface $F(t)$ (in N) against time t (in s), computed for shallow water (blue) and Benney-Luke (orange) according to equation (12).

$$g = 9.81\text{m/s}^2,\ N_x = 10,\ N_y = 50,\ Z_0 = 0.056\text{m},$$
$$R_c = R_i = 202.3\text{V/A},\ n_q = 1,$$
$$L_i = 0.35\text{Nm/A}^2,$$

and the coil winding number taken is $n_c = 2889$. The simulation time is generally $T = 10$s, such that it is longer than 10 wave periods T_p with $T_p = 2\pi/\omega_i$. The standard simulation has $N_n = 621$ nodes and 555 elements. The BL model has higher-order, more accurate dispersive terms than the shallow water model, explaining differences seen in the respective simulations.

The wavemaker output and resulting free-surface evolution at $y = 0$ can be seen in Fig. 3, for a set of simulations using the same parameters but based on the shallow water or Benney-Luke systems. Note that till time $t = 2$ there is no reflection, at $t = 4$, reflections reach the wavemaker, and at $t = 6$ the (partially) reflected waves from the wavemaker impact the buoy again. On the one hand, these counter reflections at the wavemaker are interfering; on the other hand, at sea reflections from the breakwater and device will be present as well, making the wavetrain more irregular, here at later times. Fig. 4 presents the generated current $I(t)$ and power $P_g(t) = R_l I(t)^2$ from the same simulation set, while Fig. 5 shows the integrated pressure on the buoy which yields the force $F(t)$ imposed by the water pressure on the buoy's surface, i.e.

$$F(t) = \rho_0 \int_0^{L_x} \int_{L_b}^{l_y} \lambda \,\mathrm{d}y\,\mathrm{d}x. \tag{12}$$

The mathematical and numerical models conserve energy except for the in/outflux rate of energy O_w via the waves generated by the wavemaker or entering/leaving the domain plus the rate of energy loss P_l in the electrical circuits and the power (rate of wave-energy) P_g harvested, stored in batteries or – here– used in the power-absorbing (LED-)loads. The energy balance reads: $\mathrm{d}E/\mathrm{d}t = -P_l - P_g + O_w$, with $P_l = (R_c + R_i)I^2$ and $P_g = R_l I^2$. In the shallow-water case $O_w = R\int gH_0\,\eta|_{y=0}\,\mathrm{d}x$. The integrated loss or power over time is defined as: $(\hat{P}_l, \hat{P}_g) = \int_0^T (P_l, P_g)\,\mathrm{d}t$. The numerically computed energy of the shallow-water and Benney-Luke systems are shown in Figs. 6 and 7, respectively, including the respective energies of the three subsystems (water, buoy, and electromagnetic system). Before the wavemaker is shut off energy oscillations converge to a fixed profile and thereafter the energy does converge towards a constant value. Simulations with twice the spatial resolution at $N_x = 20, N_y = 100$ agree within a few percent for the shallow-water system but are seen to *diverge* for the BL-system. Apparently, the numerical consistency of the constraints needs to be met at machine precision rather than at 10^{-6}. The power lost or generated in the shallow-water and BL simulations are given in Figs. 8 and 9, respectively, for a range of wavemaker frequencies and amplitudes. Remarkable is the reduction of resonance frequencies in the BL-simulations as well as the slight reduction in power, the latter which is due to less energy having been released into the system via the wavemaker, see Figs. 6, 7.

V. Conclusion

Further investigations have been undertaken regarding the modelling of a new wave-energy device involving a wave-activated buoy and an electromagnetic generator in a V-shaped contraction. Several improvements have been made to the (numerical) model formulations, augmented with the identification and analysis of a dispersive Benney-Luke (BL) wave model of interim complexity, in addition to probing preliminary simulations of the linearised BL wave-energy

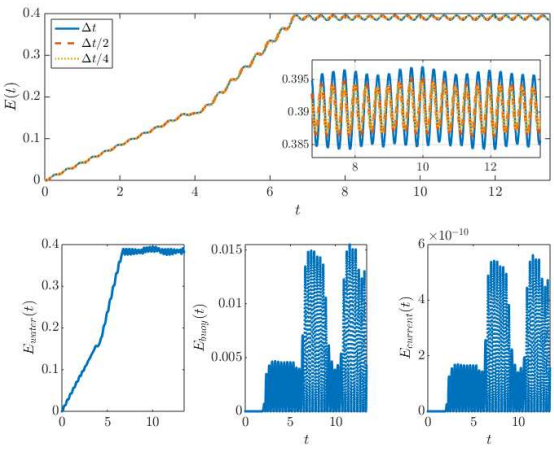

Fig. 6. Energy evolution over time t (in s) for overall energy E and energies E_{water}, E_{buoy} and $E_{current}$ (all in J) of the three subsystems for a shallow-water simulation. Mean energy for $t > T_w$ is 0.39J. $A = 0.0653$m and $\omega = 9.33$Hz. Energy for time-steps $\Delta t, \Delta t/2, \Delta t/4$; $N_x = 10, N_y = 50$. (Inset panel shows time convergence).

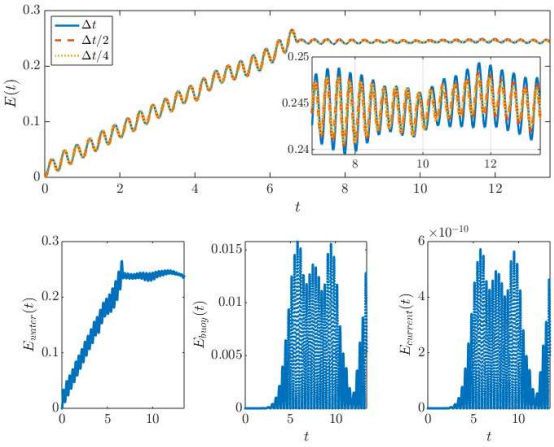

Fig. 7. Energy evolution over time t (in s) for overall energy E and energies E_{water}, E_{buoy} and $E_{current}$ (all in J) of the three subsystems for a BL-simulation. Mean energy for $t > T_w$ is about 0.245J. $A = 0.0653$m and $\omega = 9.33$Hz. Energy for time-steps $\Delta t, \Delta t/2, \Delta t/4$; $N_x = 10, N_y = 50$. (Inset panel shows time convergence).

system. Unfortunately, the numerics of the BL-system diverges most likely because the consistency in the continuum model could not be met in the numerics, due to the coupling with the wave-buoy, in contrast to novel proofs for the shallow-water model as well as the potential-flow model (details of which are omitted for brevity). The recommendation is therefore to continue with the potential flow model to capture wave dispersion, where a lower resolution in the vertical direction can be taken if computational speed needs to be maintained, which would be similar to a BL-system with its quadratic velocity potential profile in the vertical but without the numerical inconsistencies. Alternative higher-order 2D models such as Boussinesq models or modified BL-systems are another option.

The device is best situated in a breakwater to lower construction and maintenance costs by combining and

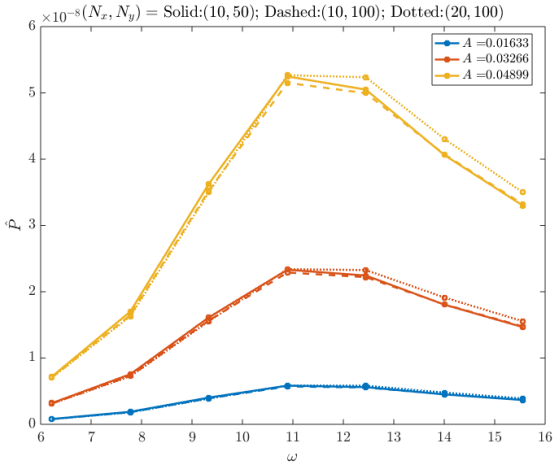

Fig. 8. Generated power (in Volt×Ampere) as function of wavemaker frequency ω for three wavemaker amplitudes A for the non-dispersive linearised shallow-water system, over $T = 10$s, at various resolutions. Resonance at circa 11Hz.

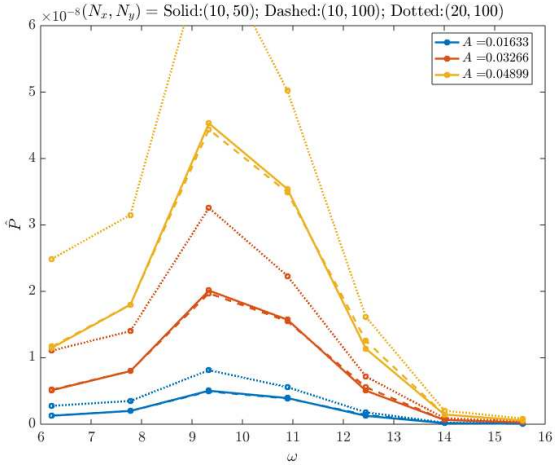

Fig. 9. Generated power (in Volt×Ampere) as function of wavemaker frequency ω for three wavemaker amplitudes A for the dispersive linearised Benney-Luke system, over $T = 10$s. Resonance at circa 9.33Hz. The solution eventually diverges.

altering the normal wave-obstructing function of a breakwater with the damping of waves by the generation of electromagnetic power.

In the design stage of a wave-energy device, simplified linear models are often used to optimise and control the device's performance. However, maximising the power output often requires the device's motion to be magnified, violating the underlying small-amplitude assumption of the linearisation. This contradiction has been deemed a modelling paradox [19]. In practice, in wavetanks and at sea, wave-energy devices are subjected to strong nonlinear effects, be that hydrodynamic, mechanical or electromagnetic. Such nonlinearities are clearly notable in the nonlinear models of the present device (in the 2D BL system (6)) and in the 3D potential-flow equations given in [4], [5].

To address this paradox, several studies have employed a (pseudo-)two-phase Navier-Stokes-based hydrodynamic model in an attempt to analyse both linear and nonlinear effects, and quantify the severity of the

contradiction [19], [20]. Alternatively, nonlinear wave models of interim complexity, such as the one used in the present work, are advocated for use in (nonlinear) optimisation and control, owing to their computational cheapness relative to Navier-Stokes-based models.

The formulation of the weakly nonlinear wave model (either a 3D potential-flow model with low or high resolution in the verical direction) and the implementation and consistent numerical formulation of its linearisation carried out here constitute the necessary first steps towards building this framework. Subsequent steps are as follows: (i) to perform further optimisation of the device's output with respect to static parameters such as the tank dimensions, buoy mass and electromagnet size and strength, and to investigate the scope for real-time control by varying dynamic parameters such as the loading and induction-coil characteristics; (ii) to adapt the current numerical framework to solve the nonlinear potential-flow model with wave-breaking parameterisation for improved optimisation and control; and (iii) to validate the analytical and numerical work against laboratory tests, initially at the scales used in the presented simulations.

Regarding (ii), the mathematical model allows an overall coordinate transformation to be carried out, as in [21], [22], such that the moving nonlinear boundaries $y = R(t)$ and $y = y_b(x,t)$ become fixed and the hydrodynamic sub-domains in both the linear and nonlinear models become equivalent. While the numerical framework for the nonlinear model will require additional features (i.e. iterative solvers) to deal with the nonlinear hydrodynamic and geometric terms (the latter arising from the coordinate transformation), the methodologies developed here will remain valid. The use of *Firedrake* will facilitate this development [18].

In summary, the wave-modelling approach followed here is a step towards the creation of a multi-fidelity surrogate nonlinear modelling approach, where most of the computational work needed to create surrogate models of the performance objectives can be based on cheaper 2D or vertically low-resolution 3D wave modelling. These efficiency gains will, in turn, facilitate optimisation of the device's power output, subject to practical operating constraints, within feasible timescales. Finally, regarding survivability, the device can be sunken off in severe weather, cf. [8], or contracting walls can be slanted such that high waves can escape onto the continued break water, thus protecting the device, by limiting its amplitude.

REFERENCES

[1] A. Falcão, "Wave energy utilization: a review of the technologies," *Renew. Sust. Energ. Rev.*, vol. 14, no. 3, pp. 899–918, 2010.

[2] S. Salter, "The swinging mace," in *Proceedings of the Workshop on Wave Energy R&D*, Cork, Ireland, 1992, pp. 197–206.

[3] E. Mehlum, "TapChan," in *Hydrodynamics of Ocean Wave-Energy Utilization*, D. Evans and A. Falcão, Eds. Berlin: Springer, 1986, pp. 51–55.

[4] O. Bokhove, A. Kalogirou, D. Henry, and G. Thomas, "A novel wave-energy device with enhanced wave amplification and induction actuator," *Int. J. Mar. Energy*, vol. 3, no. 1, pp. 37–44, 2020.

[5] O. Bokhove, A. Kalogirou, and W. Zweers, "From Bore–Soliton–Splash to a new wave-to-wire wave-energy model," *Water Waves*, vol. 1, no. 2, pp. 217–258, 2019.

[6] S. Noren, "Plant for utilizing kinetic energy," U.S. Patent No. 4277690, 7th July 1981 [Original Swedish Patent No. 7808679, 16th August 1978].

[7] P. Boccotti, P. Filianoti, V. Fiamma, and F. Arena, "Caisson breakwaters embodying an OWC with a small opening. Part II: a small-scale field experiment," *Ocean Eng.*, vol. 34, no. 5-6, pp. 820–841, 2007.

[8] F. Mahdi and R. Yeung, "On survivability of asymmetric wave-energy converters in extreme waves," *Renew. Energ.*, vol. 119, pp. 891–909, 2018.

[9] O. Bokhove and W. Zweers. (2016) Video of wave-energy device. Youtube. [Online]. Available: https://www.youtube.com/watch?v=SZhe_SOxBWo&ab_channel=AnnaKalogirou

[10] M. Penalba and J. Ringwood, "A review of wave-to-wire models for wave energy converters," *Energies*, vol. 9, p. 506, 2016.

[11] R. Haftka, D. Villanueva, and A. Chaudhuri, "Parallel surrogate-assisted global optimization with expensive functions – a survey," *Struct. Multidiscip. O.*, vol. 54, no. 1, pp. 3–13, 2016.

[12] S. Li and B. Ke, "Study of battery modeling using mathematical and circuit oriented approaches," in *2011 IEEE Power and Energy Society General Meeting*, Detroit, MI, USA, 2011.

[13] D. Benney and J. Luke, "On the interactions of permanent waves of finite amplitude," *J. Math. Phys. Camb.*, vol. 43, no. 1-4, pp. 309–313, 1964.

[14] R. Pego and J. Quintero, "Two-dimensional solitary waves for a Benney–Luke equation," *Physica D*, vol. 132, p. 476–496, 1999.

[15] O. Bokhove and A. Kalogirou, "Variational water wave modelling: from continuum to experiment," in *Lecture Notes on the Theory of Water Waves*, M. G. T. Bridges and D. Nicholls, Eds. London Mathematical Society Lecture Notes Series 426, 2016, pp. 226–259.

[16] A. O'Sullivan and G. Lightbody, "Co-design of a wave energy converter using constrained predictive control," *Renew. Energy*, vol. 102, pp. 142–156, 2017.

[17] E. Hairer, C. Lubich, and G. Wanner, *Geometric Numerical Integration*, 2nd ed. Berlin: Springer, 2006.

[18] F. Rathgeber, D. Ham, L. Mitchell, M. Lange, F. Luporini, A. McRae, G.-T. Bercea, G. Markall, and P. Kelly., "Firedrake: automating the finite element method by composing abstractions," *ACM T. Math. Software*, vol. 43, no. 3, pp. 24:1–24:27, 2016.

[19] C. Windt, N. Faedo, M. Penalba, F. Dias, and J. Ringwood, "Reactive control of wave energy devices – the modelling paradox," *Appl. Ocean Res.*, vol. 109, p. 102574, 2021.

[20] C. Windt, J. Davidson, and J. Ringwood, "Numerical analysis of the hydrodynamic scaling effects for the Wavestar wave energy converter," *J. Fluid. Struct. Submitted*, 2021.

[21] A. Engsig-Karup, H. Bingham, and O. Lindberg, "An efficient flexible-order model for 3D nonlinear water waves," *J. Comput. Phys.*, vol. 228, no. 6, pp. 2100–2118, 2009.

[22] F. Gidel, "Variational water-wave models and pyramidal freak waves," Ph.D. dissertation, University of Leeds, 2018, https://etheses.whiterose.ac.uk/21730/.

[23] J. Luke, "A variational principle for a fluid with a free surface," *J. Fluid Mech.*, vol. 27, no. 2, pp. 395–397, 1967.

[24] J. Miles, "On Hamilton's principle for surface waves," *J. Fluid Mech.*, vol. 83, no. 1, pp. 153–158, 1977.

[25] C. Cotter and O. Bokhove, "Variational water-wave model with accurate dispersion and vertical vorticity," *J. Eng. Math.*, vol. 67, pp. 33–54, 2010.

[26] E. Gagarina and O. Bokhove, "On variational and symplectic time integrators for hamiltonian systems." *J. Comp. Phys.*, vol. 306, pp. 370–389, 2010.

APPENDIX A
VARIATIONAL PRINCIPLE

The variational principle used to derive equations (6) is given by $\mathcal{S} \equiv \int_0^T \mathcal{L}[\mathbf{v}]\,\mathrm{d}t$, with arbitrary end-point $t = T$, $\mathbf{v} = (h, \Phi, \lambda, Z, W, P_Q, Q)$ the vector of unknowns and Lagrangian $\mathcal{L}(t)$ of the system, defined as

$$\mathcal{L}[\mathbf{v}] = \rho_0 \int_0^{L_x}\int_R^{l_y} \Bigg\{ h\frac{\partial \Phi}{\partial t} - \frac{H_0^2 h}{2}\frac{\partial}{\partial t}\left(\nabla^2\Phi\right) + \frac{h}{2}\|\nabla\Phi\|^2 + \frac{H_0^3}{3}\left(\nabla^2\Phi\right)^2 + \frac{gh(h-2H_0)}{2}$$

$$+\lambda(h-h_b)\Theta(y-y_b)\Big\}\,\mathrm{d}y\,\mathrm{d}x$$
$$-MW\dot{Z}-P_Q\dot{Q}+\frac{1}{2}MW^2$$
$$+MgZ+\frac{1}{2}\frac{(P_Q+K(Z))^2}{L_i}. \tag{A.1}$$

The equations satisfy the variation of $\mathcal{S}$ given by

$$\delta\mathcal{S}\equiv\lim_{\varepsilon\to 0}\left[\frac{1}{\varepsilon}\int_0^T\left\{\mathcal{L}[\mathbf{v}+\varepsilon\delta\mathbf{v}]-\mathcal{L}[\mathbf{v}]\right\}\,\mathrm{d}t\right]=0,$$

where $\delta\mathbf{v}$ denotes an arbitrary change in $\mathbf{v}$. For more details and examples of this process, see [23]–[25].

Appendix B
Discretisation and weak forms

Using the superscripts n and $n+1$ to denote values at the n^{th} and $(n+1)^{\text{th}}$ time-step, the symplectic (or semi-implicit) Euler scheme [17, p. 189] is applied to pairs of conjugate variables $\{\mathbf{p},\mathbf{q}\}$, and is given by

$$\frac{\mathbf{p}^{n+1}-\mathbf{p}^n}{\Delta t}=f_{\mathbf{p}}(\mathbf{p}^{n+1},\mathbf{q}^n),\ \frac{\mathbf{q}^{n+1}-\mathbf{q}^n}{\Delta t}=f_{\mathbf{q}}(\mathbf{p}^{n+1},\mathbf{q}^n).$$

So, $\mathbf{p}^{n+1}$ is first calculated implicitly using $\mathbf{p}^{n+1}$ and $\mathbf{q}^n$ on the RHS, and then $\mathbf{q}^{n+1}$ is computed explicitly using $\mathbf{q}^n$ and the obtained $\mathbf{p}^{n+1}$. In the present system, the three variable pairings are $\{\Phi,\eta\}$, $\{W,Z\}$ and $\{P_Q,Q\}$, with $\mathbf{p}=(\Phi,W,P_Q)$ and $\mathbf{q}=(\eta,Z,Q)$.

To be consistent, appropriate weak forms of the coupled system of consistency relations must be exclusively derived from the basic weak forms, as well as the ODEs involved. Weak forms arise as follows. First, an additional test function $\hat{\varphi}=\varphi\Theta(y-L_b)$ is defined on $y>L_b$ under the buoy, such that $\hat{\varphi}(x,y)=0$ on $y\le L_b$. This ensures that (the restriction of) $\nabla\varphi$ at $y=L_b$ is defined and finite. Second, the basis functions for λ are chosen to smoothly extend one layer of elements for $y<L_b$ with $\lambda=0$ at any key nodes $y<L_b$ or faces not connected to nodes on $y=L_b$, see Fig. 2. Furthermore, $\lambda(x,L_b,t)$ is given by (9i). This ensures that $\nabla\lambda$ is defined at $y=L_b$ as well.

Given the above-outlined time-stepping scheme and the constraint nature of the system, the complete time-discrete weak forms and ODEs, solved either within Matlab or with Firedrake, are as follows, in which double integrals concern $0\le x\le L_x$, $0\le y\le l_y$ and single integrals $0\le x\le L_x$,

Waterline BC:

$$\lambda^n=g(\eta^n|_{y=L_b}-Z^n)\ \text{ at }\ y=L_b, \tag{B.1a}$$

Consistency conditions, i.e. system for λ and $\partial q/\partial t$:

$$\iint\Big\{H\nabla\hat{\varphi}\cdot\nabla\lambda^n+\frac{\hat{\varphi}\rho_0}{M}\iint\lambda^n\,\mathrm{d}y\,\mathrm{d}x$$
$$+\underline{H_0^2\left(\frac{3H}{4}-H_0\right)\nabla\hat{\varphi}\cdot\nabla\left(\frac{q^{n+1}-q^n}{\Delta t}\right)}$$
$$-\frac{\hat{\varphi}\gamma G(Z_0)I^n}{M}+gH\nabla\hat{\varphi}\cdot\nabla\eta^n\Big\}\,\mathrm{d}y\,\mathrm{d}x=0 \tag{B.1b}$$
$$\iint\Big\{\varphi\frac{(q^{n+1}-q^n)}{\Delta t}+\underline{\frac{H_0^2}{2}\nabla\varphi\cdot\nabla\left(\frac{q^{n+1}-q^n}{\Delta t}\right)}$$
$$+\frac{2}{3}\nabla\varphi\cdot\nabla\left\{\lambda^n+g\eta^n\right\}\Big\}\,\mathrm{d}y\,\mathrm{d}x$$
$$-\frac{2}{3}\int\varphi|_{y=0}\frac{(\dot{R}^{n+1}-\dot{R}^n)}{\Delta t}\,\mathrm{d}x=0, \tag{B.1c}$$

Remaining time-stepping equations:

$$\iint\Big\{\varphi\frac{(\Phi^{n+1}-\Phi^n)}{\Delta t}+\underline{\frac{H_0^2}{2}\nabla\varphi\cdot\nabla\left(\frac{\Phi^{n+1}-\Phi^n}{\Delta t}\right)}$$
$$+g\varphi\eta^n+\varphi\lambda^n\Theta(y-L_b)\Big\}\,\mathrm{d}y\,\mathrm{d}x$$
$$+\underline{\frac{H_0^2}{2}\int\varphi|_{y=0}\frac{(\dot{R}^{n+1}-\dot{R}^n)}{\Delta t}\,\mathrm{d}x}=0, \tag{B.1d}$$

$$\underline{\iint\left\{\varphi q^{n+1}-\frac{2}{3}\nabla\varphi\cdot\nabla\Phi^{n+1}\right\}\mathrm{d}y\,\mathrm{d}x}$$
$$\underline{-\frac{2}{3}\int\varphi|_{y=0}\dot{R}^{n+1}\,\mathrm{d}x=0}, \tag{B.1e}$$

$$(W^{n+1}-W^n)/\Delta t=-\gamma G(Z_0)I^n/M$$
$$+\frac{\rho_0}{M}\iint\tilde{\lambda}^n\Theta(y-L_b)\,\mathrm{d}y\,\mathrm{d}x, \tag{B.1f}$$

$$(Q^{n+1}-Q^n)/\Delta t=I^n, \tag{B.1g}$$

$$\iint\Big\{\varphi\frac{(\eta^{n+1}-\eta^n)}{\Delta t}+\underline{\frac{H_0^2}{2}\nabla\varphi\cdot\nabla\left(\frac{\eta^{n+1}-\eta^n}{\Delta t}\right)}$$
$$-H\nabla\varphi\cdot\nabla\Phi^{n+1}-\underline{H_0^3\nabla\varphi\cdot\nabla q^{n+1}}\Big\}\,\mathrm{d}y\,\mathrm{d}x$$
$$-H_0\int\varphi|_{y=0}\dot{R}^{n+1}\,\mathrm{d}x=0, \tag{B.1h}$$

$$(Z^{n+1}-Z^n)/\Delta t=W^{n+1}, \tag{B.1i}$$

$$L_i\frac{(I^{n+1}-I^n)}{\Delta t}=\gamma G(Z_0)W^{n+1}$$
$$-\frac{1}{2}(R_c+R_i+R_l)(I^{n+1}+I^n). \tag{B.1j}$$

The equation (B.1b) includes a slight abuse of notation, given that we have extended λ one layer of elements into the free-surface area. The above can be reformulated by defining a new variable $\mu_v(x,y,t)=\lambda(x,y,t)-g(\eta(x,y,t)-Z)$ or $\mu_v(x,y,t)=\lambda(x,y,t)-g(\eta(x,L_b,t)-Z)$ such that $\mu_v(x,L_b,t)=0$, with further accompanying finite-element approximations.

Consistency relations (B.1b) and (B.1c) are obtained by eliminating variables evaluated at time level $(n+1)$ of the weak form of the maintained constraint, i.e.

$$\iint\tilde{\hat{\varphi}}(\eta^{n+1}-Z^{n+1})\,\mathrm{d}y\,\mathrm{d}x=0, \tag{B.2}$$

while using the weak forms above in (B.1) in which updates of these variables are defined. For the BL system, it is not possible to show numerical consistency, while numerical consistency is now proven for both the shallow-water model and the linear potential flow model.

Note that the current I is modelled to ensure a symmetric time discretisation of the dissipative term, as in (B.1j), see [26] (their Fig. 9). The above discretisation yields $P_Q^{n+1}=P_Q^n$ when dissipation $R_t\equiv R_c+R_i+R_l=0$, i.e. it is consistent with $\dot{P}_Q=0$ when $R_t=0$.